Numerical Heat Transfer, Part B, 48: 425–444, 2005

ISSN: 1040-7790 print/1521-0626 online
DOI: 10.1080/10407790500274364

Taylor & Francis
Taylor & Francis Group

NUMERICAL MODELING FOR MULTIPHASE INCOMPRESSIBLE FLOW WITH PHASE CHANGE

Xiao-Yong Luo, Ming-Jiu Ni, Alice Ying, and M. A. Abdou
Mechanical & Aerospace Engineering Department, University of California, Los Angeles, Los Angeles, California, USA

A general formula for the second-order projection method combined with the level set method is developed to simulate unsteady, incompressible multifluid flow with phase change. A subcell conception is introduced in a modified mass transfer model to accurately calculate the mass transfer across the interface. The third-order essentially nonoscillatory (ENO) scheme and second-order semi-implicit Crank-Nicholson scheme is employed to update the convective and diffusion terms, respectively. The projection method has second-order temporal accuracy for variable-density unsteady incompressible flows as well. The level set approach is employed to implicitly capture the interface for multiphase flows. A continuum surface force (CSF) tension model is used in the present cases. Phase change and dynamics associated with single bubble and multibubbles in two and three dimensions during nucleate boiling are studied numerically via the present modeling. The numerical results show that this method can handle complex deformation of the interface and account for the effect of liquid–vapor phase change.

1. INTRODUCTION

The heat transfer and incompressible flow processes associated with phase-change phenomena are typically among the complex transport circumstances encountered in engineering applications, such as power and refrigeration cycles, petroleum and chemical processing, thermal control of aircraft avionics and spacecraft environments, and operating circumstances of nuclear power plant design. These processes may have complexities including nonlinearities, time-varying behavior, dynamic interaction between the phases, and motion of the interface. Theoretical and experimental studies have laid the necessary groundwork for the phase change, but it is clear that computational modeling can provide accurate predictions of physical phenomena with complex interactions among many effects such as fluid flow, surface tension, and heat and mass transfer with phase change. However, accurate numerical investigation to predict the associated heat and mass transfer has often proved to be a formidable task. Computations of this problem are still far behind what is possible for multifluid flows without phase change. Typical numerical

Received 31 March 2005; accepted 21 May 2005.

The authors would like to thank Prof. S. Osher for fruitful discussion. This work is supported by the U.S. Department of Energy under Grant DE-FG03-86ER52123.

Address correspondence to Xiao-Yong Luo, UCLA MAE Department, 44-136 Engineering IV, Los Angeles, CA 90095-1597, USA. E-mail: xyluo@ucla.edu

models use an assumed interface shape or do not consider flows in which the interface deforms greatly [1]. Various simplifications concerning surface tension, fluid viscosity, vapor-phase velocity, and temperature are also usually made. Advanced numerical technique was first employed by Son et al. [2] for boiling by using a level set method to capture interface, and a projection method to solve the incompressible Navier-Stokes equations. In their computation, the temperature inside the boiling bubble is assumed to be constant. Mass transfer across the interface is decided by the temperature gradient at the liquid side of the interface. Welch and Wilson [3] applied a volume-of-fluid (VOF) method to capture the interface, while the mass transfer model in [3] is the same as the model in [2]. Juric and Tryggvason [4] applied a front tracking method for the interfacial flows, in which they also build up an implicit relationship between mass transfer and interface temperature model. This relationship is further used to get an iteration formula to calculate the interface temperature and mass transfer across the interface. Jamet et al. [5] developed a method for phase change based on second gradient theory, which is a phase-field-like method, in which the liquid–vapor interface is described as a three-dimensional continuous medium. Across the interface, the physical properties are continuous.

Primitive-variable numerical methods, including the MAC method [6], the projection method [7–11], the SIMPLE method [12, 13], and others, are usually employed to conduct the computation of incompressible Navier-Stokes equations. Kothe and Mjolsness [14] conducted the computation of interfacial flows by using the MAC method, in which the explicit updating of the convective and diffusion terms is not stable with a big time-step size. Chen et al. [15] employed the SIMPLE method for the numerical simulation of bubble rising flows. Son et al. [2] employed the projection method to do numerical simulation of boiling heat transfer, which incorporates the level set approach for capturing the interface. SIMPLE-type methods have been proven to have second-order temporal accuracy [16]. However, the first-order full implicit scheme is employed to update the convective and diffusion terms in [15]. In [2], the first-order fully explicit and fully implicit schemes are employed to update the convective and diffusion terms, respectively. The temporal accuracy of the methods in both [15] and [2] is only first-order. Ni et al. [17] developed a general four-step or three-step Runge–Kutta Crank–Nicholson (RKCN) projection method for unsteady incompressible single-phase flows and extended it to solve variable-density incompressible interfacial flows [18]. In this article we extend the RKCN method to simulate the free surface with phase-change problem to investigate the bubble growth pattern during fully nucleate boiling and multibubble interaction. The numerical methodology is conducted by using the second-order projection method, in conjunction with approximate factorization (AF) for incompressible Navier-Stokes equations [19]. The vapor–liquid interface is captured by a level set method [20] which can easily handle breaking and merging of the interface. A three-order essentially monoscillatory (ENO) scheme [21] is used for the convective term to guarantee the accuracy of the method and the Crank-Nicholson method is used for the diffusion term to eliminate the numerical viscous stability restriction. Furthermore, a ghost fluid method (GFM) [22], incorporated to deal with the discontinuity boundary, more accurately simulating heat and mass transfer at the interface, will be described later.

Employing the variable-density projection method and the level set method to simulate immiscible interfacial flows with phase change is the main subject of this article. The physical models, a modified mass transfer model, and numerical algorithms are presented in Section 2. The broken-dam validation case is presented in Section 3. 2-D single-bubble growth pattern during nucleate boiling, 2-D multibubble dynamic interaction during nucleate boiling, and 3-D single-bubble nucleate boiling are studied numerically in Section 4. Conclusions are presented in Section 5.

2. PHYSICAL MODELS AND NUMERICAL ALGORITHMS

2.1. Governing Equations

For incompressible multiphase flows with phase change, the governing equations can be written as

$$\nabla \cdot \mathbf{u} = \frac{\mathrm{Ja}}{\mathrm{Pe}} \left[\frac{\widetilde{K}}{\widetilde{\rho}^2} ([\nabla T]_\Gamma \cdot \nabla \widetilde{\rho}) \right] \tag{1}$$

$$\frac{\partial \mathbf{u}}{\partial t} + \nabla \cdot (\mathbf{u}\mathbf{u}) = -\frac{1}{\widetilde{\rho}} \nabla p + \left(\frac{1}{\mathrm{Fr}} - \frac{\mathrm{Gr}}{\mathrm{Re}^2} T \right) \mathbf{g} + \frac{1}{\widetilde{\rho}\ \mathrm{Re}} \nabla \cdot (\widetilde{\mu} \nabla \mathbf{u}) + \frac{1}{\widetilde{\rho}\ \mathrm{Re}} \nabla \cdot (\widetilde{\mu} \nabla \mathbf{u})^T + \frac{k(\phi)\delta(\phi)\nabla\phi}{\widetilde{\rho}\ \mathrm{We}} \tag{2}$$

$$\frac{\partial T}{\partial t} + \mathbf{u} \cdot \nabla T = \frac{1}{\widetilde{\rho}\widetilde{C}_p} \frac{1}{\mathrm{Pe}} [\nabla \cdot (\widetilde{K} \nabla T)] \tag{3}$$

where

$$[\nabla T]_\Gamma = (\nabla T)_{\text{liquid}} - (\nabla T)_{\text{gas}} \tag{4}$$

with dimensionless groups of Reynolds, Froude, Weber, Jacob, Peclet, and Grashof numbers,

$$\mathrm{Re} = \frac{\rho_l U L}{\mu_l} \qquad \mathrm{Fr} = \frac{U^2}{gL} \qquad \mathrm{We} = \frac{\rho_l U^2 L}{\sigma} \qquad \mathrm{Ja} = \frac{Cpl(T_w - T_{sat})}{h_{fg}}$$

$$\mathrm{Pe} = \frac{\rho_l U L C_{pl}}{K_l} \qquad \mathrm{Gr} = \frac{g_0 L^3 \rho_l^2 \beta_l (T_w - T_s)}{\mu_l^2}$$

Here U and L are characteristic velocity and length, respectively; σ is the surface tension coefficient; $\widetilde{\mu} = \mu/\mu_l$, $\widetilde{\rho} = \rho/\rho_l$, $\widetilde{K} = K/K_l$, and $\widetilde{C_p} = C_p/C_{pl}$ are the dimensionless viscosity, density, thermal conductivity, and specific heat. ϕ is the level set function, k is the front curvature of the interface, and δ is the smeared-out Dirac delta function. A continuum surface force (CSF) model [23, 24] is used to reformulate the surface tension as a volume force.

2.2. Level Set Method

The level set method [20] is employed to capture the interface implicitly by introducing a smooth level set function ϕ, with the zero level set as the interface, positive value outside the interface, and negative value inside the interface. Consider the following interface evolution equation:

$$\frac{\partial \phi}{\partial t} + \mathbf{u} \cdot \nabla \phi = 0 \tag{5}$$

which will evolve the zero level of $\phi = 0$ exactly as the actual interface moves. The corresponding physical variants can be expressed as

$$\widetilde{\rho}_{\xi}(\phi) = \lambda_{\rho} + (1 - \lambda_{\rho}) H_{\xi}(\phi) \tag{6}$$

$$\widetilde{\mu}_{\xi}(\phi) = \lambda_{\mu} + (1 - \lambda_{\mu}) H_{\xi}(\phi) \tag{7}$$

where $\lambda_{\rho} = \rho_g/\rho_l$ and $\lambda_{\mu} = \mu_g/\mu_l$. H is the smeared-out Heaviside function defined by

$$H(\phi) = \begin{cases} 0 & \phi < -\varepsilon \\ \dfrac{1}{2} + \dfrac{\phi}{2\varepsilon} + \dfrac{1}{2\pi} \sin\left(\dfrac{\pi\phi}{\varepsilon}\right) & -\varepsilon \le \phi \le \varepsilon \\ 1 & \phi < \varepsilon \end{cases} \tag{8}$$

where ε is a tunable parameter that determines the size of the bandwidth of numerical smearing. A typical good value is $\varepsilon = 1.5\,\Delta x$; see Figure 1.

Since ϕ will generally drift away from its initialized value as the signed distance while Eq. (5) will move the level set $\phi = 0$ with the correct velocity, a reinitialization approach based on solving the hyperbolic partial differential equation is presented in [25, 26]. The reinitialization equation is

$$\phi_t = L(\phi_0, \phi) = S_{\varepsilon}(\phi_0)(1 - |\nabla \phi|) \tag{9}$$

$$\phi_t = L(\phi_0, \phi) + \lambda f(\phi) \tag{10}$$

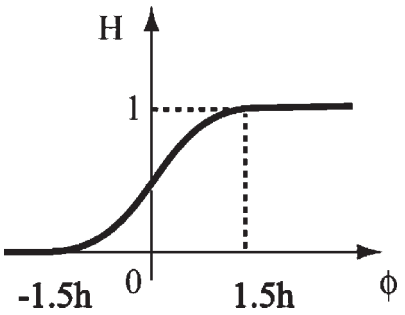

Figure 1. Smoothing of the Heaviside function.

where λ is a local constraint and function of t only, determined by

$$\lambda = \frac{-\int_\Omega H'(\phi) L(\phi_0, \phi)}{\int_\Omega H'(\phi) f(\phi)} \tag{11}$$

where

$$f(\phi) = H'(\phi)|\nabla\phi| \tag{12}$$

2.3. Variable-Density RKCN Projection Method

Ni et al. [17] developed a general four-step or three-step RKCN projection method for unsteady incompressible single-phase flows and extended it to solve variable-density incompressible interfacial flows [18]. In this article we extend the RKCN method to simulate the interfacial phase change with heat and mass transfer. The variable-density RKCN projection method for phase change can be expressed as

$$A^m \hat{\mathbf{u}}^m = r^m - \frac{\alpha^m \nabla p^{m-1} + \beta^m \nabla p^{m-2}}{\widetilde{\rho}^{n+1/2}} \tag{13}$$

$$\widetilde{\vec{\mathbf{u}}}^m = \hat{\mathbf{u}}^m + \Delta t \cdot \frac{\alpha^m \nabla p^{m-1} + \beta^m \nabla p^{m-2}}{\widetilde{\rho}^{n+1/2}} \tag{14}$$

$$\alpha^m \nabla \cdot \left(\frac{\nabla p^m}{\widetilde{\rho}^{n+1/2}} \right) = \frac{1}{\Delta t} \nabla \cdot \tilde{\mathbf{u}}^m - \beta^m \nabla \cdot \left(\frac{\nabla p^{m-1}}{\widetilde{\rho}^{n+1/2}} \right) - \left(\frac{1}{\Delta t} \nabla \cdot \mathbf{u}^m \right) \tag{15}$$

$$\mathbf{u}^m = \tilde{\mathbf{u}}^m - \Delta t \cdot \frac{\alpha^m \nabla p^m + \beta^m \nabla p^{m-1}}{\widetilde{\rho}^{n+1/2}} \tag{16}$$

$$\phi^{m+1} = \phi^m - \Delta t \left(\alpha^{m+1} \mathbf{u}^m \cdot \nabla \phi^m + \beta^{m+1} \mathbf{u}^{m-1} \cdot \nabla \phi^{m-1} \right) \tag{17}$$

where

$$A^m = \frac{1}{\Delta t} \left[I - \frac{\Delta t \cdot \gamma^m}{\widetilde{\rho}^{n+1/2} \, \mathrm{Re}} \nabla \cdot \left(\widetilde{\mu}^{n+1/2} \nabla \right) \right] \tag{18}$$

$$r^m = \frac{1}{\Delta t} \left[I - \frac{\Delta t \cdot \gamma^m}{\widetilde{\rho}^{n+1/2} \, \mathrm{Re}} \nabla \cdot \left(\mu^{n+1/2} \nabla \right) \right] \mathbf{u}^{m-1} - \alpha^m [S]^{m-1} - \beta^m [S]^{m-2} \tag{19}$$

$$S = \frac{1}{\widetilde{\rho} \, \mathrm{Re}} \nabla \cdot \left[\widetilde{\mu}^{n+1/2} (\nabla \mathbf{u})^T \right] - \left(\frac{1}{\mathrm{Fr}} - \frac{\mathrm{Gr}}{\mathrm{Re}^2} T \right) g_i - \frac{k(\phi)\delta(\phi)\nabla\phi}{\widetilde{\rho} \, \mathrm{We}} \tag{20}$$

and

$$\alpha^m = \left(\frac{8}{15}, \frac{5}{12}, \frac{3}{4}\right) \qquad \beta^m = \left(0, -\frac{17}{60}, -\frac{5}{12}\right) \qquad \gamma^m = \left(\frac{4}{15}, \frac{1}{15}, \frac{1}{6}\right)$$

are coefficients of the third-order Runge-Kutta method. The velocity components and pressure in the intermediate velocities equation at the first substep are $\mathbf{u}^{-1} = 0$, $p^{-1} = 0\,(m-2=-1)$, and $\mathbf{u}^0 = \mathbf{u}^n$, $p^0 = p^n\,(m-1=0)$. At the third step they are $\mathbf{u}^3 = \mathbf{u}^n + 1$ and $p^3 = p^{n+1}$, which are the updated velocities and pressure for the next time level, $n+1$. The density, viscosity, and temperature are updated using ϕ^{n+1}, which will be $\tilde{\rho}^{n+1/2}$, $\tilde{\mu}^{n+1/2}$, and $T^{n+1/2}$ at the next time step.

In the above variable-density RKCN projection method, the Crank-Nicholson implicit technique is employed to update the diffusion term for stability, and the low-storage three-stage Runge-Kutta technique is employed to update the convective term for simplicity and stability. The projection method also has second-order temporal accuracy for variable-density unsteady incompressible flows. The diffusion term can be spatially discretized using standard central difference schemes. The convective term in the momentum equation can be conveniently updated using the third-order ENO scheme [21].

2.4. A Modified Mass Transfer Model

Mass transfer during the phase-change process is associated with the temperature and density gradient near the interface, as we can see from the governing equation (1). Son et al. [2] simplify it by assuming the gas side is always at saturation temperature, so that only the temperature gradient on the liquid side is accounted for in the mass transfer. The mass continuity and energy balance at the interface with evaporation are expressed as

$$\mathbf{m} = \tilde{\rho}(\mathbf{u}_{\text{int}} - \vec{u}) = \frac{\tilde{k}\nabla T}{h_{fg}} \tag{21}$$

Assuming that the interface is advected the same way as the level set function, the continuity equation can be rewritten as

$$\nabla \cdot \mathbf{u} = \frac{\mathbf{m}}{\tilde{\rho}^2} \cdot \nabla\tilde{\rho} = \frac{\tilde{k}\nabla T}{h_{fg}\tilde{\rho}^2} \cdot \nabla\tilde{\rho} \tag{22}$$

with its dimensionless form

$$\nabla \cdot \mathbf{u} = \frac{\text{Ja}}{\text{Pe}}\left(\frac{k\nabla T}{\tilde{\rho}^2}\right) \cdot \nabla\tilde{\rho} \tag{23}$$

This simplified model is physically pretty accurate when simulating nucleate boiling phenomena. However, the following discretization formula,

$$\left(\frac{\partial T}{\partial x}\right)_{\text{across interface}} = \frac{T_{i+1} - T_I}{\Delta x} \tag{24}$$

for the calculation of the temperature gradient will cause great error when dealing with complex heat and mass transfer conditions, since the mass transfer is dependent on the difference of the temperature gradients on both sides of the phase interface. Unfortunately, the numerical results of [2] and [3] are acquired based on the model of Eqs. (23) and (24). For the VOF method [27], it is not so convenient to accurately discretize the gradients on both sides of the free interface, since the volume fraction is discontinuous. However, for the level set method, it will be shown that we can accurately discretize the temperature gradient very conveniently, since the level set function is a distance function from the front interface. In this article, we modify this mass transfer model by introducing a subcell concept to accurately calculate the temperature gradient on both sides in the gas–liquid phase-change region. The modified mass transfer model greatly improves the numerical results and is a general model for liquid–gas phase-change heat and mass transfer.

Since the interface usually has a fairly complex shape, the level set representation of the interface is used in this work. Assuming the interface lies between the nodes i and $i+1$, the temperature at these nodes are T_i and T_{i+1}, respectively (see Figure 2).

Taking the subcell location of the interface into account allows us to discretize the temperature gradient more accurately. Suppose that $\phi_i \leq 0$ and $\phi_{i+1} > 0$. Define a θ function to estimate the subcell interface location:

$$\theta = \frac{|\phi_i|}{|\phi_i| + |\phi_{i+1}|} \tag{25}$$

The interface splits this cell into two pieces of size $\theta\,\Delta x$ on the left and size $(1-\theta)\,\Delta x$ on the right. Denoting the temperature value at this subcell interface location by T_I, which is given by the physical properties, and discretize the temperature gradient near the interface as

$$\left(\frac{\partial T}{\partial x}\right)_{\text{liquid}} = \frac{T_{i+1} - T_I}{(1-\theta)\,\Delta x} \qquad \left(\frac{\partial T}{\partial x}\right)_{\text{gas}} = \frac{T_I - T_i}{\theta\,\Delta x} \tag{26}$$

For the Y and Z normal directions, the procedure is the same so that we can get all three values of the temperature gradient near the interface. Considering the

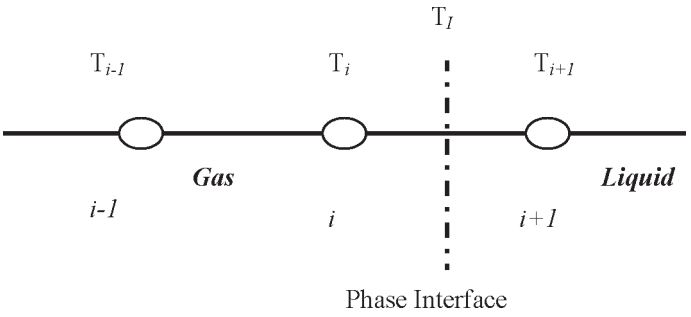

Figure 2. Phase interface location.

mass continuity and energy balance at the interface with phase change, we can modify Eq. (23) as Eq. (1),

$$\nabla \cdot \mathbf{u} = \frac{\mathrm{Ja}}{\mathrm{Pe}} \left[\frac{\widetilde{K}}{\widetilde{\rho}^2} ([\nabla T]_\Gamma \cdot \nabla \widetilde{\rho}) \right] \tag{1}$$

where

$$[\nabla T]_\Gamma = (\nabla T)_{\text{liquid}} - (\nabla T)_{\text{gas}} \tag{4}$$

Once the first derivative of the temperature has been computed, the second derivative of the temperature across the interface can be computed as follows. We define

$$(KT_x)_{i+1/2} = K^- \left(\frac{T_I - T_i}{\theta \, \Delta x} \right) \tag{27}$$

and

$$(KT_x)_{i-1/2} = K^- \left(\frac{T_i - T_{i-1}}{\theta \, \Delta x} \right) \tag{28}$$

arriving at

$$\frac{\partial}{\partial x} (KT_x)_i = \frac{(KT_x)_{i+1/2} - (KT_x)_{i-1/2}}{\Delta x} \tag{29}$$

The formula of Eqs. (1) and (4) coupling with the numerical models of Eqs. (26)–(29) will be called the subcell model, and the original model of Eqs. (23) and (24) will be called the old model later in this article.

3. NUMERICAL SIMULATION OF VALIDATION CASES

The broken dam problem is calculated to further validate the code by comparing the numerical result with the experimental data. An 81×41 uniform Cartesian grid is used with initial water column height-to-width ratio of 2. $\rho_{\text{water}}/\rho_{\text{back}} = 1,000$, $\mu_{\text{water}}/\mu_{\text{back}} = 1,000$, and $\mathrm{Re} = 1,000$. At the outlet boundary, the Neumann boundary condition is set for velocities. At all other boundaries, slip wall boundary conditions are applied for the velocities. Figure 3 illustrates the free surface profiles between time = 0.2 and time = 3.0 with time interval of 0.2. The water surface evolves in a smooth shape and no oscillation occurs at the interface near the solid wall.

Figure 4*a* shows the history of the waterfront moving along the ground surface ($y = 0$), and Figure 4*b* shows the transient height of the wetted wall along the vertical surface ($x = 0$). The error bar in Figure 4*a* shows the interface height in this calculation. The experimental results from Martin and Moyce (1952) are also shown in Figure 4. The numerical results match the experimental data well.

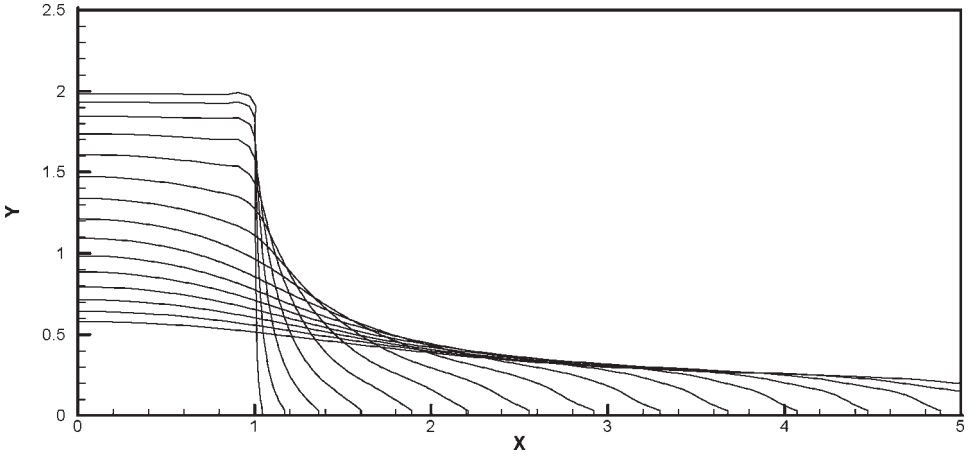

Figure 3. Zero level set contour from time = 0.2 to time = 3.0.

4. NUMERICAL SIMULATION OF BUBBLES DURING NUCLEATE BOILING

4.1. 2-D Single-Bubble Nucleate Boiling

The 2-D single-bubble computational domain is 1×2 and the meshes are 57×103. The initial bubble radius is 0.1. The Reynolds number is 100 and the Weber number is 5. The density ratio is $\rho_l/\rho_g = 1,000/1$ and the viscosity ratio is $\mu_l/\mu_g = 100/1$. To initiate the computations, the initial fluid temperature profile is taken to be linear in the natural-convection thermal boundary layer and fluid velocity is set equal to zero. The initial thermal boundary layer thickness is assumed to be 0.9 in this case.

Figure 5*a* shows the bubble growth pattern with time when there is no heat and mass transfer. Figures 5*b* and 5*c* show the bubble growth pattern with time by using the old model and new model separately when $\Delta T = 6.2$ K. Compared with no heat and mass transfer, the bubble grows fast when under the thermal boundary layer. After that, the bubble grows slowly and begins to break into smaller bubbles. Because of the convection initialized by the bubble movement, the temperature above the thermal boundary layer is superheated instead of saturated. Thus the heat and mass transfer still occur when the bubble is above the thermal boundary layer, although they are much smaller than under the thermal boundary layer. By using the modified model, the mass transfer part has been simulated more accurately, so that the bubble grows faster than in the old model.

Figure 6 shows the bubble mass change with time by using two different models. By using the modified model, the bubble mass increases 463.6%, compared with 248.5% in the old model. This is because the modified model considers the interface condition more accurately and thus can simulate the mass transfer part more accurately.

Figure 7 shows the single-bubble growth pattern and temperature field during the nucleate boiling by using the old and modified models. Comparing them, we can see the modified model captures more information at the interface so that the mass increases faster and the bubble holds its shape better. This is because the subcell

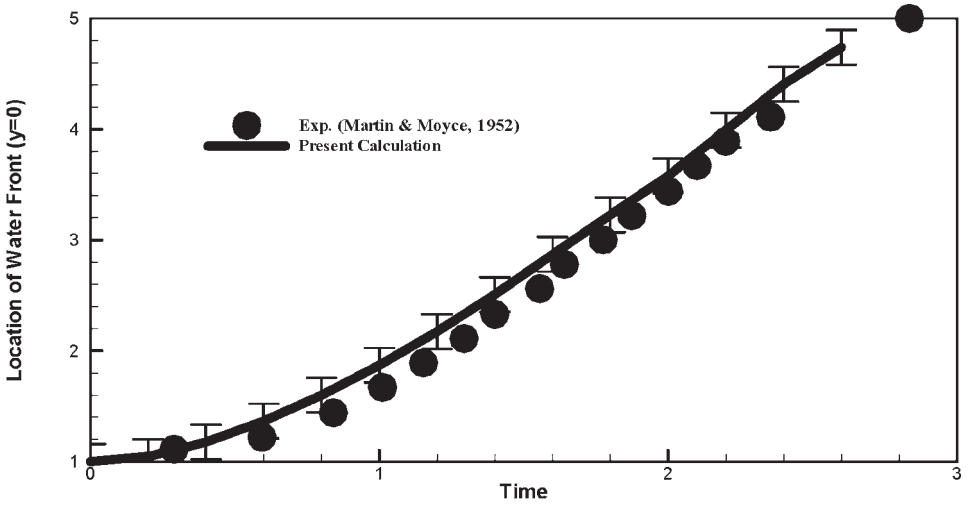

(a) Location of water front at y=0

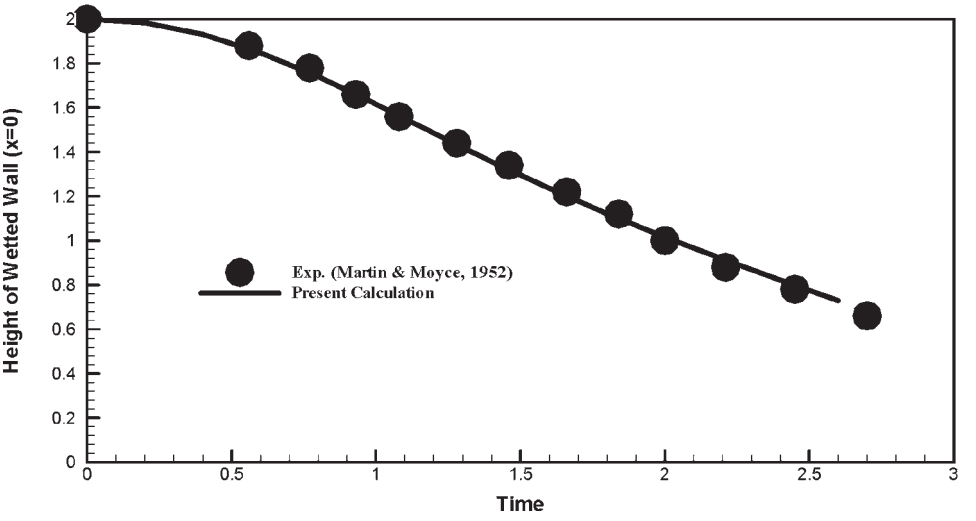

(b) Height of wetted wall at x=0

Figure 4. History of water front location on solid surfaces in the dam break.

conception has been used near the interface in the modified model and the mass transfer part can be simulated more accurately, which will affect the other terms, such as surface tension.

4.2. 2-D Multibubble Dynamic Interaction during Nucleate Boiling

The 2-D multibubbles computational domain is 2×2 and the meshes are 193×193. The initial bubble radius is 0.1. The Reynolds number is 100 and the

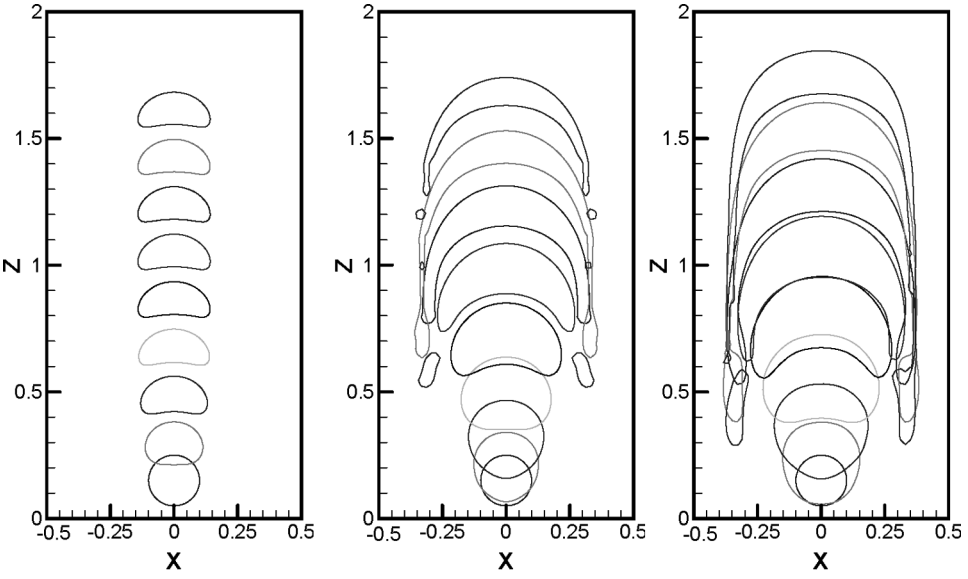

Figure 5. Comparison of single-bubble growth pattern.

Weber number is 2. The density ratio is $\rho_l/\rho_g = 1,000/1$ and the viscosity ratio is $\mu_l/\mu_g = 100/1$. To initiate the computations, the initial fluid temperature profile is taken to be linear in the natural-convection thermal boundary layer and fluid velocity is set equal to zero. The initial thermal boundary layer thickness is assumed to be 1.

In the first case, the initial positions of the two bubbles are $(-0.5, 0.15)$ and $(0.5, 0.15)$. Figure 8 shows the bubble growth pattern with time when $\Delta T = 6.2$ K. Since the Weber number is pretty small, the surface tension force is large enough to prevent the bubble to break into small bubbles. The hot vapor pushes the growing bubble upward while the colder liquid descends toward the bottom wall. Because of convection, the temperature above the thermal boundary layer is superheated instead of saturated. Thus the heat and mass transfer occurs when the bubble is still above the thermal boundary layer. Two wakes appear behind each bubble, clearly demonstrated by experiment [27].

Figure 9 shows the bubble mass change with the computational steps. With the heat and mass transfer, the bubble mass increases by four times over the initial condition. The bubble's mass increases much faster in the first 10,000 steps than later. This is because a large temperature gradient exists in the thermal boundary layer.

In the second case, the initial positions of the two bubbles are $(-0.25, 0.15)$ and $(0.25, 0.15)$. The two bubbles are closer than in the previous case in order to see the interaction between these two bubbles during the heat and mass transfer.

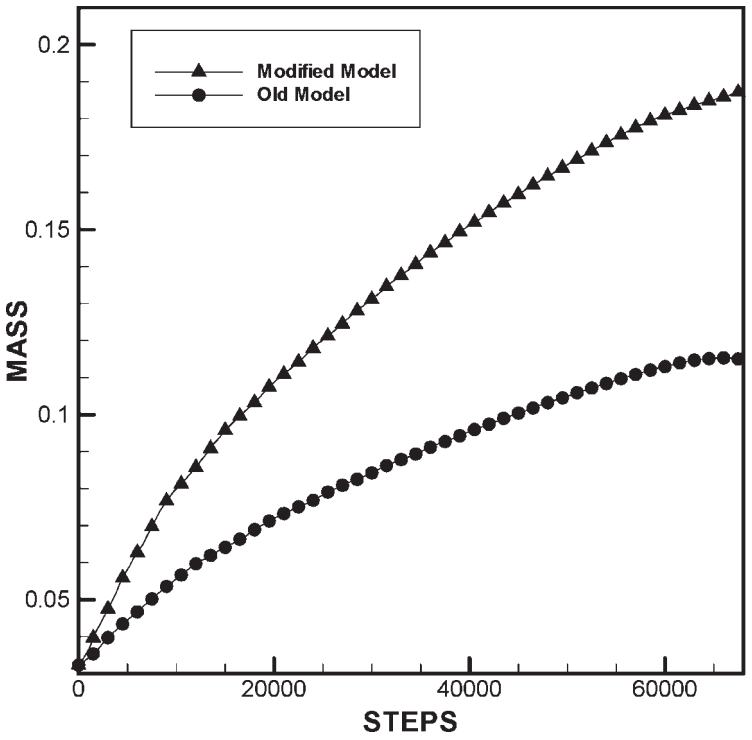

Figure 6. Steps–mass comparison between two models.

Figure 10 shows the bubbles' growth pattern with time when $\Delta T = 6.2$ K. During the processing, the hot vapor pushes the growing bubble upward while the colder liquid descends toward the bottom wall. Because of the viscous fluid, bubble motion will induce a vortex of the same sign in the computational domain. This vortex pair accelerates the separation of the bubbles. The bubbles break into smaller bubbles when outside the thermal boundary. The lower parts of the broken bubbles in the thermal boundary layer grow faster because of the large temperature gradient.

Figure 11 shows the bubble mass change with the computational steps. With the heat and mass transfer, the bubble mass increases by three times over the initial condition.

4.3. 3-D Single-Bubble Nucleate Boiling

The 3-D single-bubble computational domain is $1 \times 1 \times 2$ and the meshes are $41 \times 41 \times 81$. The initial bubble radius is 0.1. The Reynolds number is 100 and the Weber number is 5. The density ratio is $\rho_l/\rho_g = 1,000/1$ and the viscosity ratio is $\mu_l/\mu_g = 100/1$. To initiate the computations, the initial fluid temperature profile is taken to be linear in the natural-convection thermal boundary layer and fluid velocity is set equal to zero. The initial thermal boundary layer thickness is assumed to be 1 in this case.

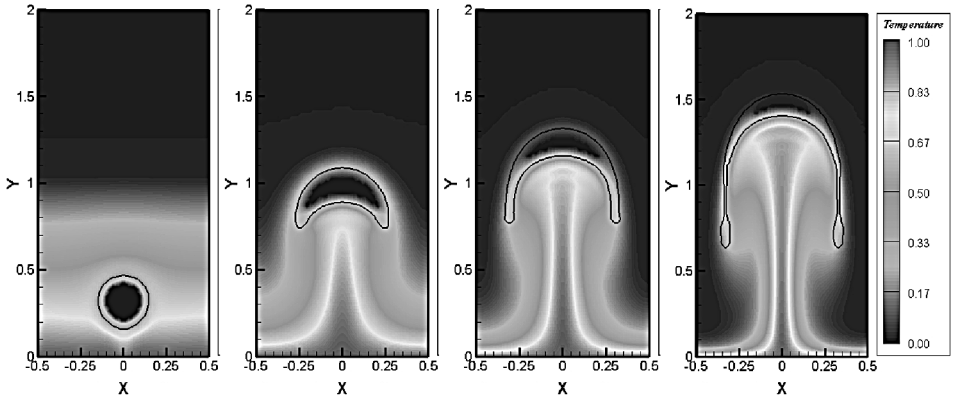

(a) Simulation results by old model

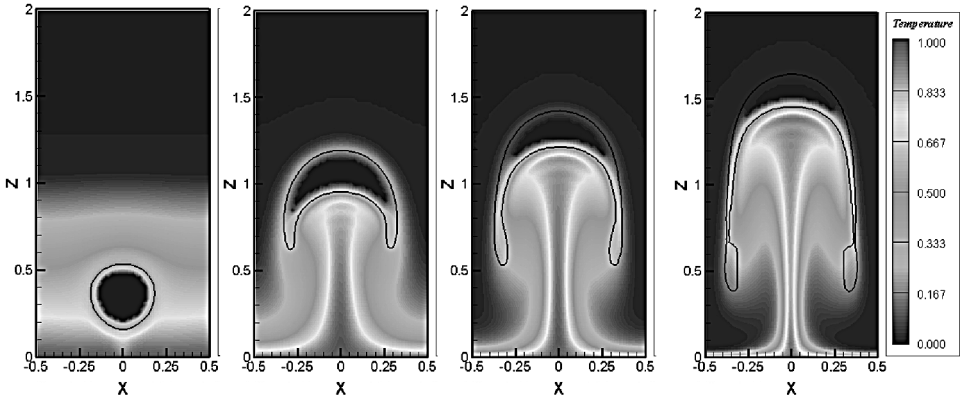

(b) Simulation results by new model

Figure 7. Single-bubble growth pattern during nucleate boiling process.

Figure 12*a* shows the bubble growth pattern when $\Delta T = 6.2$ K. With the heat and mass transfer, the bubble grows fast. When the bubble is above the thermal boundary layer, it begins to deform from the top center. The deformation propagates along the radial direction and finally the bubble breaks up and forms a corolla shape. This is significantly different from a no heat and mass transfer bubble rising, when the bubble shape holds because of a large surface tension force. If we take a look at the shape of the bubble from the bottom view, we find that the inside of the bubble became empty during the bubble expansion. When the surface tension cannot maintain this "empty inside" bubble shape, the deformation begins.

Figure 12*b* shows the bubble mass change with time by using two different models. By using the modified model, the bubble mass increases 1945.3% compared with 1089.5% in the old model. This is because the new model considers the interface condition more accurately and can simulate the mass transfer part more accurately.

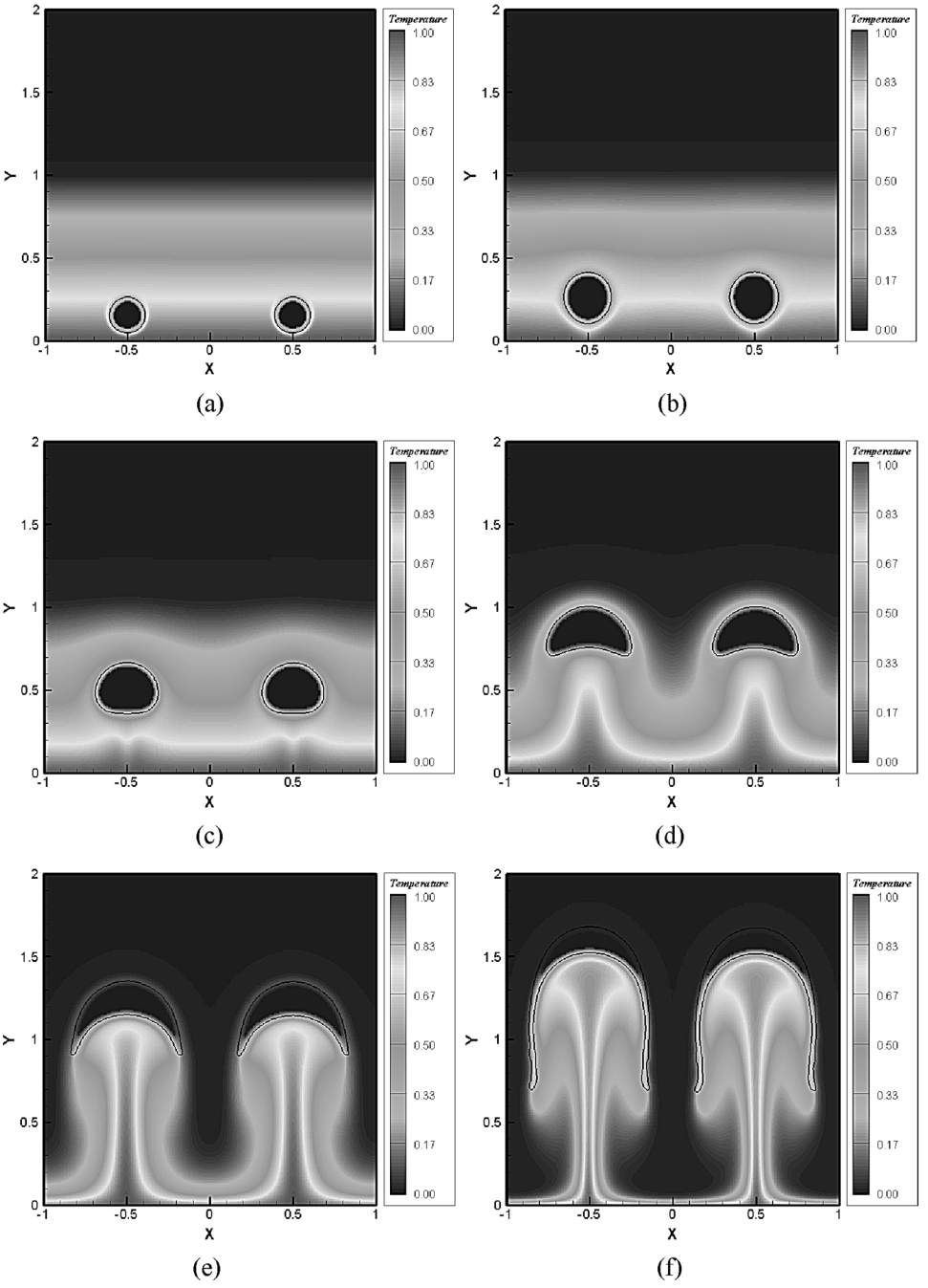

Figure 8. Two separate bubbles' growth pattern during nucleate boiling.

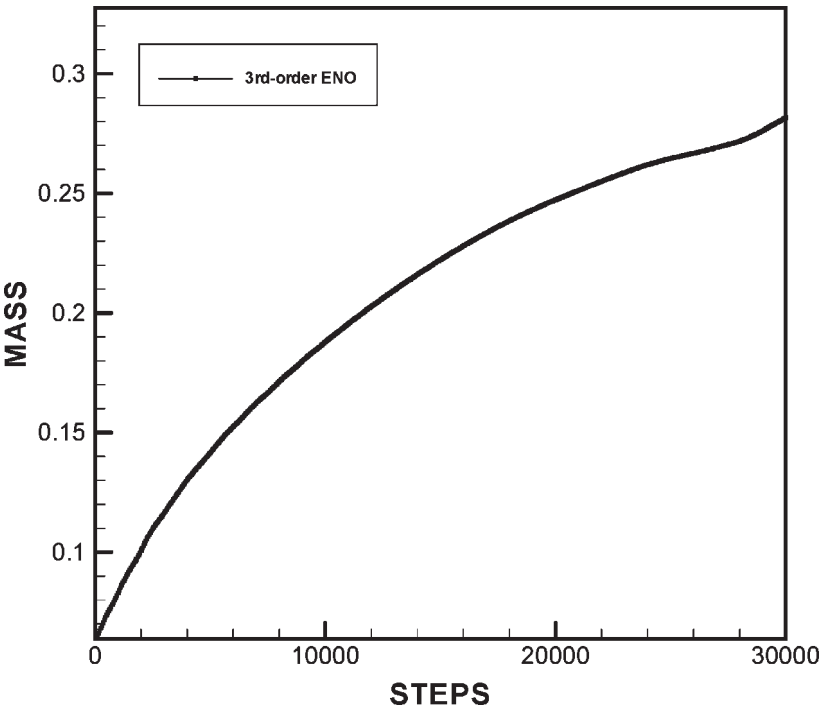

Figure 9. Bubble mass changes with computational steps.

Figure 13 shows the bubble growth pattern and temperature field contours during the nucleate boiling process by using both the old and the modified models. After the bubble deformation, the mass begins to decrease a little because the rough mesh size cannot capture smaller bubbles. When the bubble is under the thermal boundary layer, the mass transfer part is big because of the large temperature gradient. When the bubble is above the thermal boundary layer, this part decreases quickly.

5. CONCLUSION

In this article we have presented a numerical modeling for multiphase incompressible flow with phase change. The subcell conception has been introduced in the new mass transfer model. The RKCN projection method has second-order temporal accuracy for variable-density unsteady incompressible flows. The third-order ENO scheme and second-order semi-implicit Crank-Nicholson scheme is employed to update the convective and diffusion terms, respectively. The hyperbolic equation for the level set function has been employed to implicitly capture the interface for multiphase flows. The four-level multigrid technique has been employed to enforce divergence-free velocity incompressible flows. The numerical results show that this method can handle complex deformation of the interface and account for the effect of liquid–vapor phase change. The modified mass transfer model is more accurate

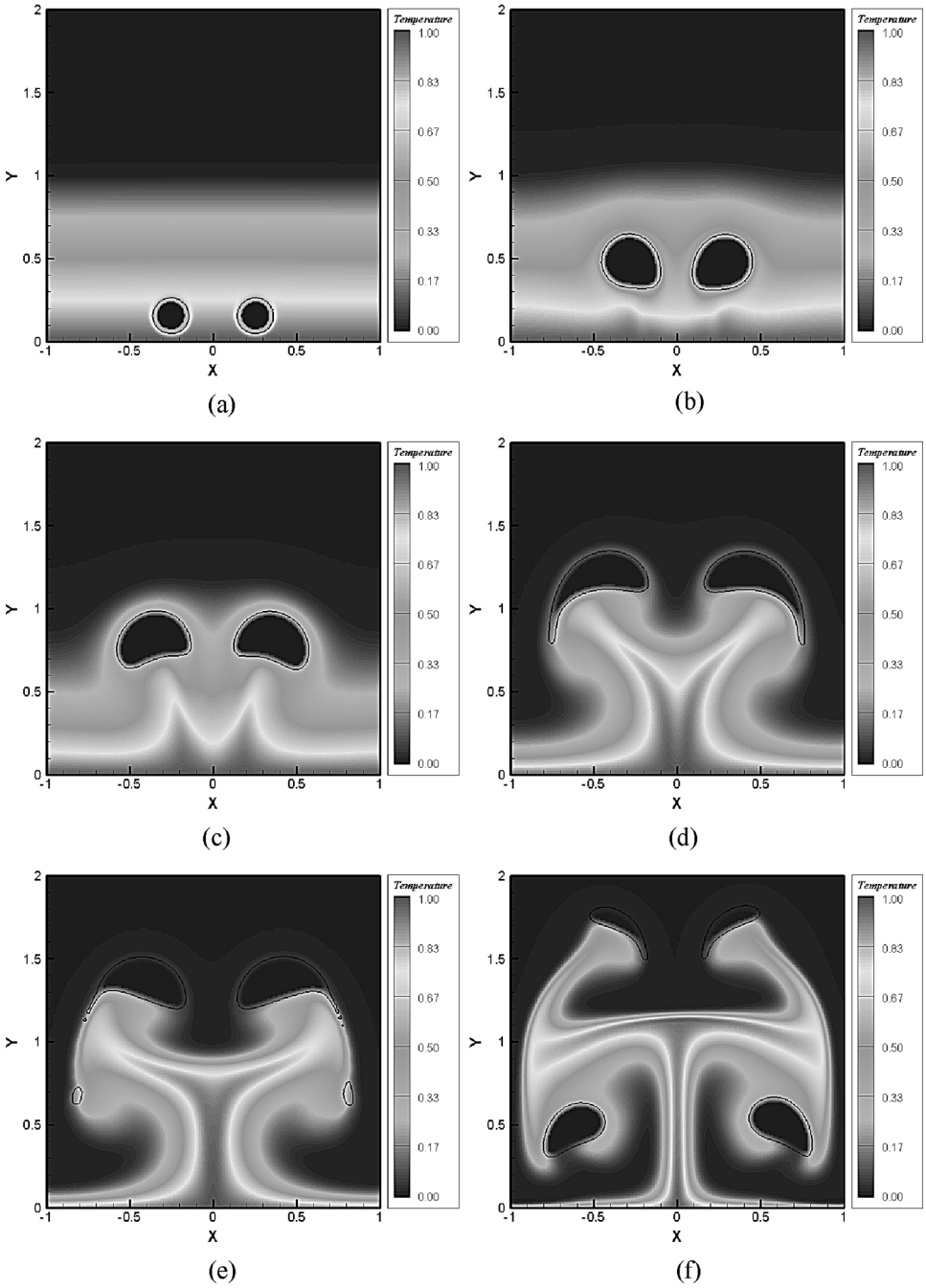

Figure 10. Two separate bubbles' growth pattern during nucleate boiling.

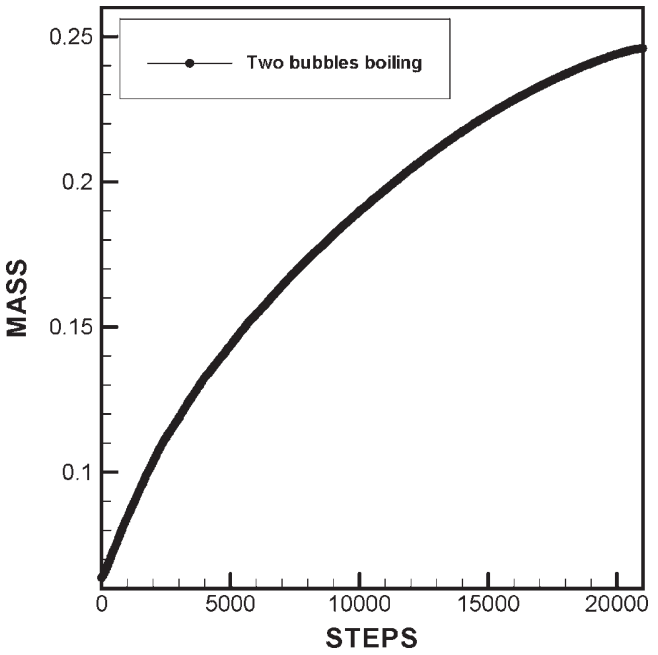

Figure 11. Bubble mass changes with computational steps.

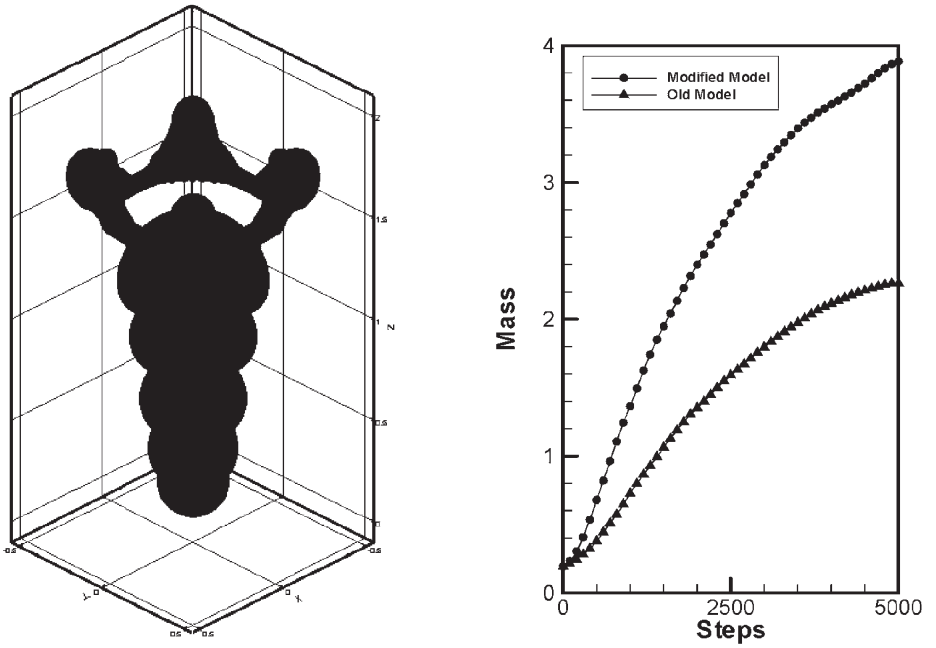

(a) Bubble growth pattern (b) Mass comparison by two models

Figure 12. 3-D bubble growth pattern when $\Delta T = 6.2$ K.

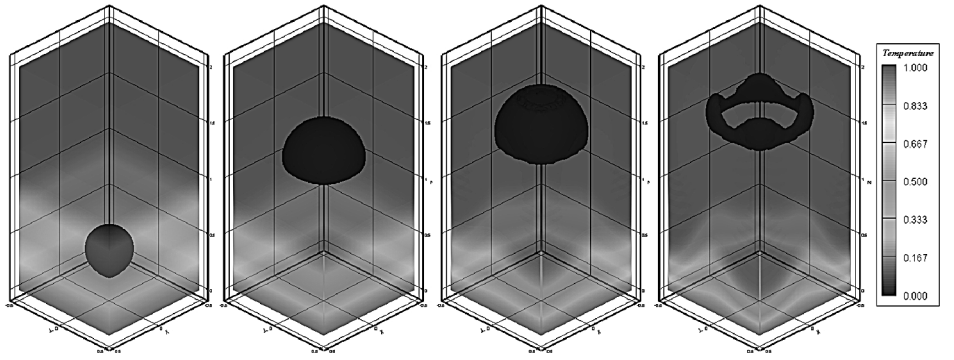

(a) Simulation results by old model

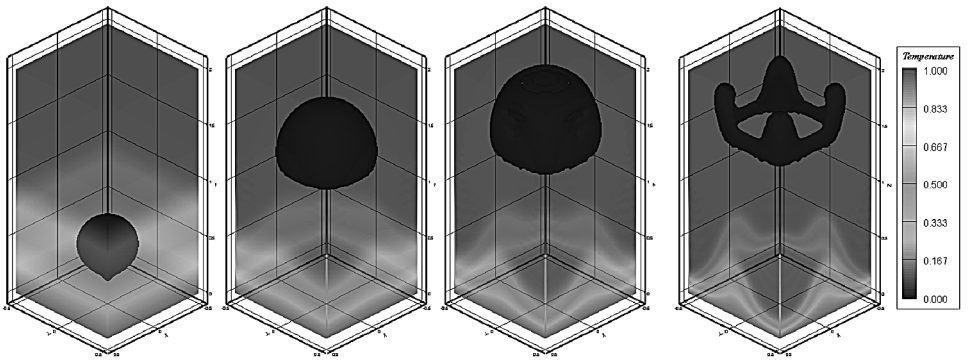

(b) Simulation results by new model

Figure 13. 3-D bubble growth pattern during nucleate boiling process.

than the old model. The present numerical modeling has been further extended by employing the ghost fluid method to calculate the heat and mass transfer at the interface. More results of multiphase incompressible flow with phase change by new modeling will be given in the future.

REFERENCES

1. P. F. Peterson, R. Y. Bai, V. E. Schrock, and K. Hijikata, Droplet Condensation in Rapidly Decaying Pressure Fields, *J. Heat Transfer*, vol. 114, pp. 194–200, 1992.
2. G. Son, V. K. Dhir, and N. Ramanujapu, Dynamics and Heat Transfer Associated with a Single Bubble during Nucleate Boiling on a Horizontal Surface, *J. Heat Transfer*, vol. 121, pp. 623–631, 1999.
3. S. Welch and J. Wilson, A Volume of Fluid Based Method for Fluid Flows with Phase Change, *J. Comput. Phys.*, vol. 160, pp. 662–682, 2000.
4. D. Juric and G. Tryggvason, Computations of Boiling Flows, *Int. J. Multiphase Flow*, vol. 24, p. 387, 1998.

5. D. Jamet, O. Lebaigue, N. Coutris, and J. M. Delhaye, The Second Gradient Theory for the Direct Numerical Simulations of Liquid-Vapor Flows with Phase-Change, *J. Comput. Phys.*, vol. 169, pp. 624–651, 2001.
6. F. H. Harlow and J. E. Welch, Numerical Calculation of Time-Dependent Viscous Incompressible Flow of Fluid with Free Surface, *Phys. Fluids*, vol. 8, no. 12, pp. 2182–2189, 1965.
7. A. J. Chorin, Numerical Solution of Navier-Stokes Equations, *J. Comput. Math.*, vol. 22, p. 745, 1968.
8. J. Kim and P. Moin, Application of Fractional-Step Method to Incompressible Navier-Stokes Equations, *J. Comput. Phys.*, vol. 59, p. 108, 1985.
9. J. B. Bell, P. Colella, and H. M. Glaz, A Second-Order Projection Method for the Incompressible Navier-Stokes Equations, *J. Comput. Phys.*, vol. 85, p. 257, 1989.
10. P. Gresho, On the Theory of Semi-implicit Projection Methods for Viscous Incompressible Flow and Its Implementation via a Finite Element Method That Also Introduces a Nearly Consistent Mass Matrix, Part I: Theory, *Int. J. Numer. Meth. Fluids*, vol. 11, pp. 587–620, 1990.
11. H. Choi and P. Moin, Effects of the Computational Time Step on Numerical Solutions of Turbulent Flow, *J. Comput. Phys.*, vol. 101, p. 334, 1992.
12. S. V. Pantankar and D. B. Spalding, A Calculation Procedure for Heat, Mass and Momentum Transfer in Three-Dimensional Parabolic Flows, *Int. J. Heat Mass Transfer*, vol. 15, p. 1787, 1972.
13. S. V. Pantankar, *Numerical Heat Transfer and Fluid Flow*, McGraw-Hill, New York, 1980.
14. D. B. Kothe and R. C. Mjolsness, IPPLE: A New Model for Incompessible Flows with Free Surfaces, *AIAA J.*, vol. 30, pp. 2694–2700, 1992.
15. L. Chen, S. V. Garimella, J. A. Reizes, and E. Leonardi, The Development of a Bubble Rising in a Viscous Liquid, *J. Fluid Mech.*, vol. 387, pp. 61–96, 1999.
16. M.-J. Ni and M. A. Abdou, Temporal Second-Order Accuracy of SIMPLE-Type Methods for Incompressible Unsteady Flows, *Numer. Heat Transfer B*, vol. 46, pp. 529–548, 2004.
17. M.-J. Ni, S. Komori, and N. Morley, Projection Methods for the Calculation of Incompressible Unsteady Flows, *Numer. Heat Transfer B*, vol. 44, pp. 533–551, 2003.
18. M.-J. Ni, S. Komori, and M. Abdou, A Variable-Density Projection Method for Interfacial Flows, *Numerical Heat Transfer B*, vol. 44, pp. 553–574, 2003.
19. J. K. Dukowicz and A. S. Dvinsky, Approximation Factorization as a High Order Splitting for Implicit Incompressible Flow Equations, *J. Comput. Phys.*, vol. 102, pp. 336–347, 1992.
20. S. Osher and J. A. Sethian, Fronts Propagating with Curvature-Dependent Speed, Algorithms Based on Hamilton-Jacobi Formulation, *J. Comput. Phys.*, vol. 79, pp. 12–49, 1988.
21. A. Harten, B. Enquist, S. Osher, and S. Chakravarthy, Uniformly High Order Essentially Non-oscillatory Schemes, *J. Comput. Phys.*, vol. 71, pp. 231–303, 1987.
22. R. P. Fedkiw, T. Aslam, B. Merriman, and S. Osher, A Non-oscillatory Eulerian Approach to Interfaces in Multimaterial Flows (the Ghost Fluid Method), *J. Comput. Phys.*, vol. 152, pp. 457–492, 1999.
23. J. U. Brackbill, D. B. Kothe, and C. Zemach, A Continuum Method for Modeling Surface Tension, *J. Comput. Phys.*, vol. 100, no. 2, pp. 335–354, 1992.
24. Y. C. Chang, T. Y. Hou, B. Merriman, and S. Osher, A Level Set Formulation of Eulerian Interface Capturing Methods for Incompressible Fluid Flows, *J. Comput. Phys.*, vol. 124, pp. 449–464, 1996.
25. M. Sussman, P. Smereka, and S. Osher, A Level Set Approach for Computing Solutions to Incompressible Two-Phase Flow, *J. Comput. Phys.*, vol. 20, pp. 1165–1191, 1994.

26. M. Sussman and E. Fatemi, An Efficient Interface-Preserving Level Set Redistancing Algorithm and Its Application to Interfacial Incompressible Fluid Flow, *J. Sci. Comput.*, vol. 20, pp. 1156–1191, 1999.
27. R. Scardovelli and S. Zaleski, Direct Numerical Simulation of Free-Surface and Interfacial Flow, *Annu. Rev. Fluid Mech.*, vol. 31, p. 567, 1999.
28. D. Bhaga and M. E. Weber, Bubbles in Viscous Liquids: Shapes, Wakes and Velocities, *J. Fluid Mech.*, vol. 105, pp. 61–85, 1981.
29. J. C. Martin and W. J. Moyce, An Experimental Study of the Collapse of Liquid Columns on a Rigid Horizontal Plane, Philosophical Transactions of the Royal Society of London. Series A, Mathe. Phys. Sci., vol. 244, pp. 312–324, 1952.